ADVANCED FUNCTIONAL MATERIALS
www.afm-journal.de

Minimize the Electrode Concentration Polarization for High-Power Lithium Batteries

Weibin Chen, Kai Wang, Yonglong Li, Jing Chen, Hongbin Wang, Liewu Li, Hao Li, Xiangzhong Ren, Xiaoping Ouyang, Jianhong Liu, Feng Pan, Biwei Xiao,* Qianling Zhang,* and Jiangtao Hu**

High-loading electrode is a prerequisite for achieving high energy density in industrial applications of lithium-ion batteries. However, an increased loading leads to elevated battery polarization and reduced battery power density, which presents a significant technical bottleneck in the industry. The present study focuses on designing a rapid electrolyte diffusion pathway to diminish lithium concentration polarization for the high-loading $LiNi_{0.83}Mn_{0.12}Co_{0.05}O_2$ (NMC83) electrode by employing two layers of NMC83 materials with different sizes. This innovative architecture demonstrates exceptional rate performance even under challenging conditions with high-loading and high-rate. Additionally, the interrelationships between electrode structure, process route, porosity, and optimal thickness ratio between layers are discussed, providing valuable guidance for industrial promotion and application. The designed L-Dry-S electrode structure (coating large particles first and then small particles) effectively mitigates concentration polarization in the thick electrode, which is attributed to the fast electrolyte diffusion channel and the differential reaction speeds of NMC83 particles with varying sizes. The knowledge from this work is broadly applicable to other material systems.

1. Introduction

Li-ion batteries (LIBs) currently dominate the portable electronic device battery market due to their high specific energy density, wide temperature range, and long cycle life.[1,2] Nevertheless, the energy density of current LIB cells cannot meet the increasing demands of the electric vehicle energy-storage market in the future. The near-term target for the automotive industry is to achieve 350 Wh kg^{-1}, while the long-term objective is to attain 500 Wh kg^{-1} at the cell level, with a lifespan exceeding 1000 cycles.[3] Among all the practical methods for constructing high-specific-energy cells, increasing the amount of active material and the thickness of the composite electrode holds promise. This approach reduces the volume of inactive components (such as current collectors, separators, and packaging) required per stack and results in high energy density and lower manufacturing costs for the batteries.

As the electrode thickness increases, lithium ions cannot be smoothly transported between the electrolyte and the active materials because of the slow and consistent ion transport process and the long transport path, resulting in a large concentration gradient on the vertical axis.[4–7] Therefore, after extended cycles, lithium ions tend to accumulate on the electrode surface, draining out in proximity of the current collector, resulting in decreased capacity and

W. Chen, H. Wang, L. Li, X. Ren, X. Ouyang, J. Liu, Q. Zhang, J. Hu
Graphene Composite Research Center
College of Chemistry and Environmental Engineering
Shenzhen University
Shenzhen 518060, P. R. China
E-mail: zhql@szu.edu.cn; hujt@szu.edu.cn

K. Wang, Y. Li
Sino-French Institute of Nuclear Engineering and Technology
Sun Yat-Sen University
Zhuhai 528478, P. R. China

K. Wang
Nuclear Professional School
School of Engineering
The University of Tokyo
2–22 Shirakata, Tokai-mura, Ibaraki 319–1188, Japan

J. Chen, X. Ouyang
School of Materials Science and Engineering
Xiangtan University
Xiangtan 411105, P. R. China

H. Li, F. Pan
School of Advanced Materials Shenzhen Graduate School
Peking University
Shenzhen 518060, P. R. China
E-mail: panfeng@pkusz.edu.cn

B. Xiao
GRINM (Guangdong) Research Institute for Advanced Materials and Technology
Foshan, Guangdong 528051, P. R. China
E-mail: xiaobiwei@grinm.com

The ORCID identification number(s) for the author(s) of this article can be found under https://doi.org/10.1002/adfm.202410926

DOI: 10.1002/adfm.202410926

poor rate and cycle performance.[2,8–11] In thick electrodes, the overall instability of the electrode structure caused by internal polarization phenomena are inherent characteristic of the traditional electrode structure.[12–14] Hence, it is necessary and substantial to design the electrode structure with high loadings. Previously, it has been demonstrated that electrode structure design plays an important role in enhancing battery electrochemical performance both experimentally and theoretically.[15,16] For instance, Wu et al.[15] built a low-tortuosity thick electrode by applying an external magnetic field, presenting uniform lithium-ion reaction kinetics inside the electrode. Nevertheless, most of the current methods require additional templates, such as ice-templating,[17,18] solvent evaporation,[19] and templated phase inversion,[20,21] and these methods usually result in a fluffy electrode with high electrode porosity. Such electrodes cannot maintain their original structure after calendaring and need more electrolytes for wetting, resulting in low energy density and significant challenges for industrial production. Furthermore, relevant reports about electrode structure design based on the traditional electrode slurry coating route is scarce.

Electrode structure design plays a crucial role in enhancing battery power performance. It has been reported that adjusting electrode tortuosity can lead to lithium batteries with high power performance. However, the conclusions derived from current electrode structure designs are not consistent. For instance, some teams believe that an electrode with high porosity at the top and low porosity at the bottom exhibits excellent overall performance.[22–26] Conversely, certain research findings suggest that flipping over such a structure yields good overall performance as well.[15] The main reason for these contradictions lies in variations in electrode loading, characteristics of the electrode material, and approaches to electrode structure design.[27] In studying electrode structure design, three requirements must be considered: high electrode loading, structural integrity after the rolling processes, and scalability potential. Based on these considerations, achieving double-layer architecture directly through the size effects of the electrode material proves more convenient.[28,29] Since a complete commercial process for designing the internal structure of thick electrodes is hardly available, this article demonstrates a detailed process for designing particle-size double-layer architecture electrodes with minimized electrode concentration polarization. We prepared double-layer coating of $LiNi_{0.83}Mn_{0.12}Co_{0.05}O_2$(NMC83) materials with different particle sizes, where the side of the current collector (bottom layer) is composed of large particles (11.3 µm) with low tortuosity, and the side close to the electrode surface (top layer) comprises small particles (4.5 µm) with high tortuosity. This electrode structure facilitates rapid electrolyte diffusion from the top to the bottom of the electrode. Coupled with the fast electrolyte diffusion channel, the intrinsic reaction speeds of the particles with different sizes are employed, which effectively alleviates the inherent concentration polarization. Moreover, the multi-layer coating techniques, electrode porosity effect, layer thickness control, *etc*. have been comprehensively studied for the preparation of high-quality electrodes. Reasonably, our designed double-layer architecture demonstrates exceptional rate performance even at extremely low porosities (< 35%). We firmly believe that the high-loading electrode with diminished cathode concentration polarization holds revolutionary significance for achieving fast charging and alleviating the range anxiety.

2. Results and Discussion

2.1. Electrolyte Infiltration Simulation and Electrochemical Characterization

There are three electrode forms (**Figure 1**a–c): L-S electrode (coating large particles first and then small particles), S-L electrodes (coating small particles first and then large particles), and Mix (mixing and coating large and small particles evenly). Here, we employed the Volume of Fluid (VOF, see details in the Experimental part) model to elucidate the diffusion mechanisms of electrolytes within the three electrode structures. As shown in Videos S1–S3 (Supporting Information), during the initial wetting stage, the air within the electrode is pushed to the surface, and pores inside the electrode are gradually occupied by an inflowing electrolyte. During the gradual infiltration of the electrolyte into the electrode to achieve an equilibrium state, the presence of nonuniform electrolyte flow and surface tension may result in the entrapment of air within pore channels. There is a gradual decrease in the value of 1% VOF from S-L electrode to Mix electrode, and then to L-S electrode (Figure 1d), indicating the presence of a rapid electrolyte infiltration pathway in the L-S electrode. Moreover, air distribution profiles are extracted from the fully submerged electrodes as shown in Figure 1e. After the electrode is wetted to a stable state, the average air fraction inside the L-S is 0.71%, significantly lower than that in S-L and Mix electrodes. This observation suggests that most pores within the L-S electrode have been filled with electrolyte and it is easier to achieve full electrolyte wetting state. The results demonstrate superior wetting performance of the L-S electrode, with only a small portion of trapped air found in bottom corners. In contrast, for S-L electrodes, narrower pores with higher tortuosity at their bottoms make it more difficult for air to escape through channels toward the top surface; consequently, air remains within a larger region of these electrodes. When the electrode surface is unwetted, the loaded active materials in those regions cannot participate in the electrochemical reactions, which results in a low specific capacity. Here, we have collected series of impedance data to validate our modeling conclusions. It has been demonstrated in related studies that the electrochemical impedance of LIBs undergoes a change during the electrolyte infiltration process. Specifically, Günter R. et al. compared the electrochemical impedance spectroscopy response signals and radiography images of cells at different stages of electrolyte wetting and determined that the Ohmic resistance *Rp*, which is the cell at the zero-crossing of the real axis in the Nyquist plot, is directly correlated with the degree of cell wetting.[30] As illustrated in Figure 1f and Figure S8 (Supporting Information), the *Rp* of L-S, Mix, S-L, L-Dry-S, Mix-Dry-Mix, and S-Dry-L all decrease with time, indicating a gradual wetting of the electrolyte. After 10 h resting, the corresponding *Rp* of L-S reached to a stable state, which was lower than that observed in the Mix and S-L (higher than 20 h). This suggests a better electrolyte wetting in the L-S and L-Dry-S electrode, followed by Mix, while S-L exhibits the least wetting and the infiltrating ability of L-S and L-Dry-S is similar.

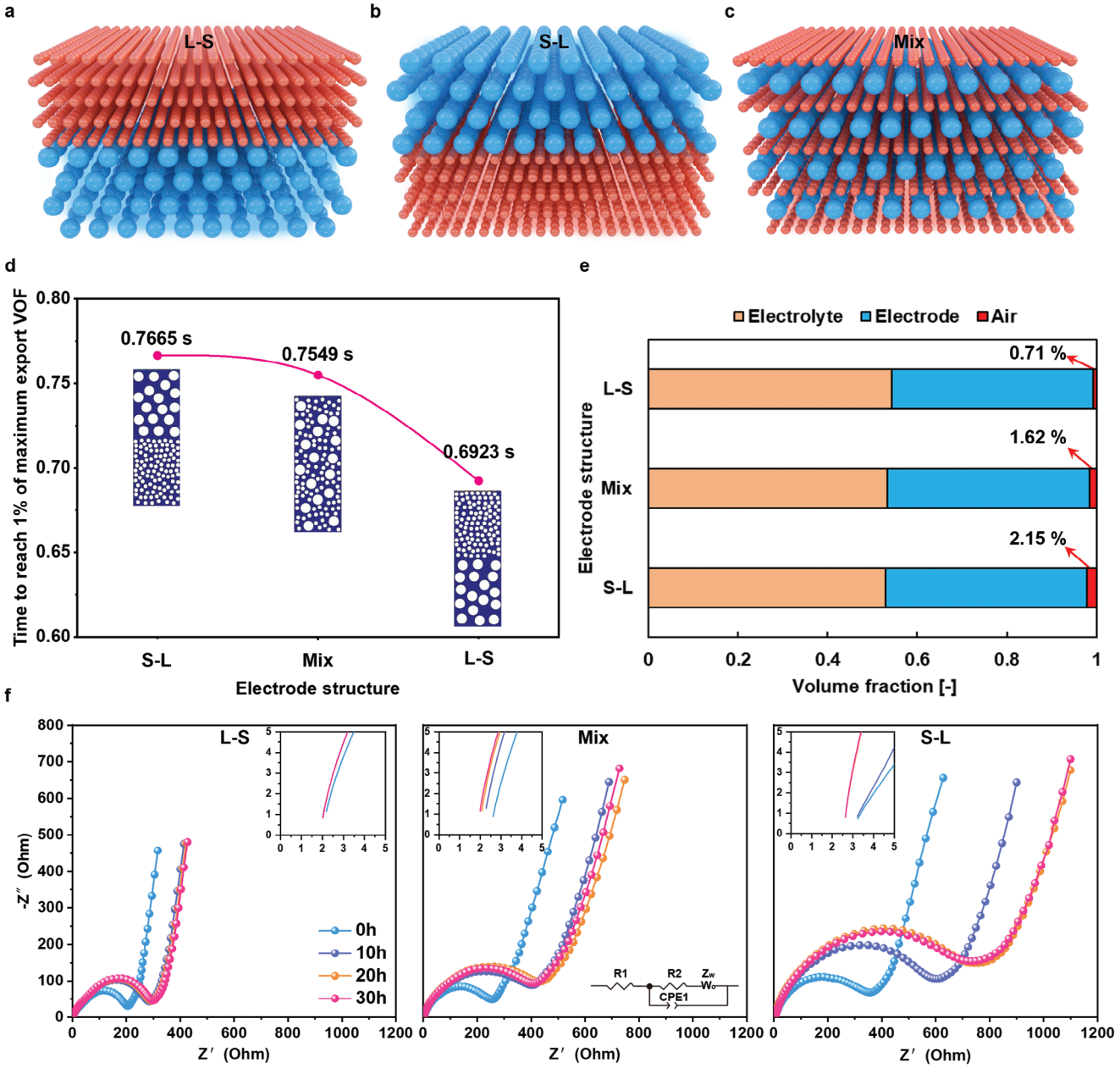

Figure 1. Particle-size double-layer architecture electrode fabrication and electrolyte infiltration simulation. a–c) Schematic diagrams of the designed electrode structures with three different arrangements: L-S (a), S-L (b), and Mix (c). d) Time to reach 1% of maximum export VOF of the three kinds of different electrodes with S-L, Mix, and L-S. e) The electrolyte, electrode, and air distribution of the three kinds of different electrodes with S-L, Mix, and L-S after electrode wetting reaches a steady-state condition. f) EIS data of L-S, Mix, and S-L during cell rest, collected by every 10 h.

2.2. Double-Layer Architecture Electrode Fabrication and Rate Capability

NMC83 particles with different sizes were utilized to prepare high-loading electrodes, and the corresponding particle sizes are 4.5 and 11.3 μm (**Figure** 2a,b). The corresponding electrode loadings of the three electrode structures are controlled at 22 mg cm^{-2} (4.6 mAh cm^{-2}) and 29.6 mg cm^{-2} (6.2 mAh cm^{-2}). The cross-sectional images of the three electrode structures under different loadings are illustrated in Figure 2c–e and Figure S1 (Supporting Information). As presented, when controlling the loading condition, we also try to ensure a comparable thickness for different layers in both L-S and S-L models.

The rate performance of the NMC cathodes with different electrode structures (Figure 2f,g) and the typical charge/discharge curves of Li||NCM83 half cells at 1C rate with areal loading is 22 and 29.6 mg cm^{-2} (Figure S9, Supporting Information) were collected to reveal the lithium-ion diffusion dynamics processes. The discharge specific capacities in the L-Dry-S and Mix-Dry-Mix models for NMC83 with a loading of 22 mg cm^{-2} are observed

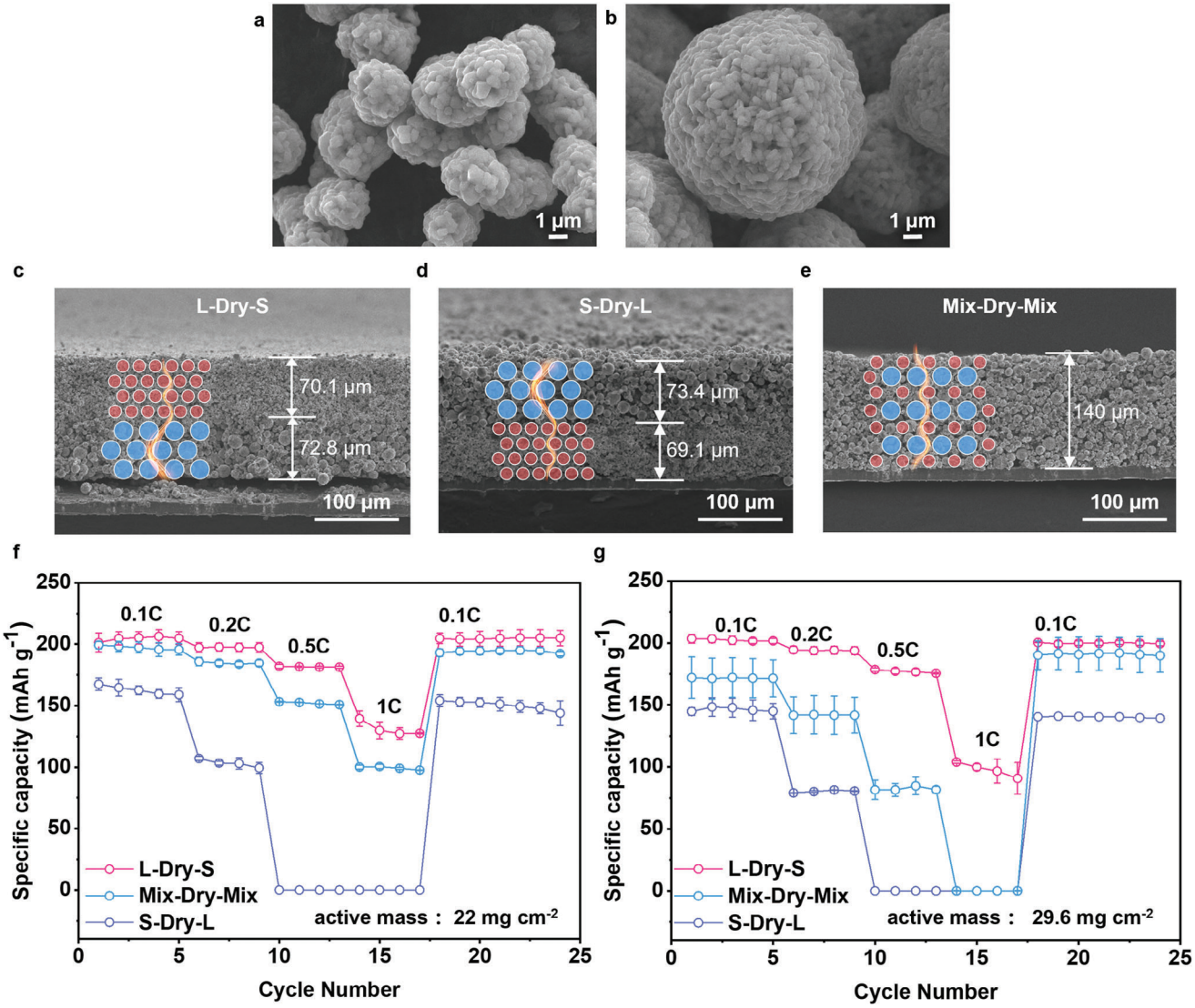

Figure 2. Double-layer architecture electrode fabrication and corresponding rate capability. a,b) Shape of small particles (a) and large particles (b). c–e) Cross-sectional images of the electrode structures for L-Dry-S (c), S- Dry-L (d), and Mix-Dry-Mix (e). The corresponding electrode loading is ≈29.6 mg cm^{-2}. f,g) Rate performance of NMC 83 electrodes (L-Dry-S, S-Dry-L, Mix-Dry-Mix) with different loadings, including 22 mg cm^{-2} (f) and 29.6 mg cm^{-2} (g). (1C = 210 mA g^{-1}).

to be higher than that in the S-Dry-L model (Figure 2f). As the current density increases, the capacity difference between these three models becomes more pronounced, particularly for the S-Dry-L model where its discharge capacity drops to zero when the current density exceeds 0.5C. As to the L-Dry-S model, it maintains the highest specific discharge capacity at 1C, which is 139.5 mAh g^{-1} higher than that in the Mix-Dry-Mix model (100.05 mAh g^{-1}). When the NMC83 electrode loading increases to 29.6 mg cm^{-2}, the L-Dry-S model electrode still performs at the best electrochemical performance (Figure 2g). The corresponding discharge capacities of L-Dry-S electrode at 0.2C, 0.5C, and 1C are 194.5, 178.55, and 103.95 mAh g^{-1}, respectively. Mix-Dry-Mix model also cannot withstand the polarization issue caused by the increased loading, and its discharge capacity at 1C is 0. Figure S9 (Supporting Information) presents the typical charge/discharge curves of Li||NCM83 half cells at 1C between 2.7 and 4.3 V. As the electrode loading increases, there is a gradual exacerbation of polarization in the electrochemical reactions, as evidenced by the progressive rise/fall in charge/discharge voltage platforms.[31–34]

It can be seen that the polarization of the Li-ion concentration in the thicker electrode is larger than that in the thinner electrode. This increased polarization indicates reduced Li-ion transport within the electrolyte, which is attributed to slower Li-ion diffusion. Consequently, under identical conditions, transportation of Li-ion to or from the active materials relies more heavily on Li-ion diffusion within the electrolyte in thicker porous electrodes than in thinner ones.[34,35]

However, it is clear that the L-Dry-S model is conducive to lithium-ion diffusion and it can alleviate the concentration polarization inherent in thick electrodes, presenting enhanced rate

performance compared with the Mix-Dry-Mix and S-Dry-L models. To further validate the internal mechanism, we conducted electrolyte diffusion rate tests (Figure S2, Supporting Information) and Li^+ diffusion coefficient (Figure S10, Supporting Information) tests on the three models. A dropwise addition of 1 M $LiPF_6$ electrolyte was performed on the three electrodes and was allowed to stand for 1 and 20 h. The diffusion rate of the electrolyte was traced using P element mapping, as shown in Figure S2 (Supporting Information).

For electrolyte diffusion rate tests, the EDS mapping after 1 hour demonstrates that the L-Dry-S and Mix-Dry-Mix electrodes exhibit higher electrolyte diffusion rates compared to the S-Dry-L electrode. After 20 h, the diffusion of the electrolyte from the surface to the bottom of all three electrodes has completed. In essence, the L-Dry-S model facilitates the diffusion of electrolytes from the surface to the interior. The electrode surface is composed of small particles with a high degree of tortuosity but are in direct contact with the electrolyte and receive a continuous supply thereof. Meanwhile, the lower part of the electrode consists of large particles that possess large voids and low tortuosity, which enable rapid transport of electrolytes.[5] The L-Dry-S design facilitates the formation of efficient electrolyte diffusion channels, and satisfies the criteria for mass and volume energy densities.

For Li^+ diffusion coefficient by electrochemical impedance spectroscopy (EIS) tests (Figure S10, Supporting Information), the elevating reversible capacity and cycling performance at large high rates are tightly associated with the Li^+ diffusion kinetic, especially considering for thick electrode with long diffusion path. Therefore, the Li^+ diffusion coefficient of L-Dry-S, Mix-Dry-Mix, and S-Dry-L at different states are very important. Nyquist plots and the corresponding profiles of Z' versus $\omega^{-1/2}$ of L-Dry-S, Mix-Dry-Mix, and S-Dry-L are displayed in Figure S10a,b (Supporting Information). Compared with L-Dry-S, Mix-Dry-Mix and S-Dry-L exhibits a slight large semicircular at the high-frequency and medium-frequency region, representing the increasing impedance of charge transfer. The slope of L-Dry-S is greater in the low-frequency region than that of Mix-Dry-Mix and S-Dry-L, contributing to the calculated smaller fitted σ value and larger $D_{Li}{}^+$ based on the formula shown in Note S1 (Supporting Information).[36] The result effectively demonstrates the intriguing kinetics of Li^+ diffusion following electrode structure control, attributing the successful optimization of electrolyte diffusion pathways and lithium-ion reaction rates in L-Dry-S to minimize electrode concentration polarization in high-power batteries. The enhanced Li^+ diffusion kinetics significantly enhance the kinetic performance of the high-loading electrodes.

2.3. Manufacturing Techniques for Double-Layer Architecture Electrodes

The preparation processes of double-layer architecture electrodes were explored. We employed two distinct routes: L-Dry-S, indicating coating a first layer of 11.3 µm large-particle NMC83 material on aluminum foil from bottom to top, followed by drying and then coating a second layer of 4.5 µm-sized NMC83 material particle; L-S, representing coating a first layer of 11.3 µm large-particle NMC83 material, followed by directly coating a second layer of 4.5 µm small-particle NMC83 material without drying (**Figure 3**a,b). For the L-Dry-S electrode structure, it can be observed that there is a clear boundary between the two layers, and the thicknesses are maintained at a 1:1 ratio. In contrast, for the L-S structure, the boundary between the first and second layers shows a mixture between the two layers, and the overall thickness is significantly smaller than that of L-Dry-S.

To further reveal the relationship between battery rate performance and electrode preparation processes, the rate performance of L-S was collected with the electrode loadings of 22 and 29.6 mg cm^{-2}. At 22 mg cm^{-2}, the specific discharge capacities of the two electrodes are not much different because sufficient time allows lithium ions to be transported from the electrolyte to the current collector.[15] As the current density increases, the electrode differences among the two different electrodes become more obvious (Figure 3c). Especially at 0.5C, L-Dry-S presents a higher discharge capacity of 182.1 mAh g^{-1} compared to the L-S electrode (142.75 mAh g^{-1}). As the NMC loading increases to 29.6 mg cm^{-2}, the specific discharge capacities of the L-Dry-S electrode at different current densities are all higher than that in the L-S electrode (Figure 3d). Moreover, S-L and Mix electrodes without drying during slurry coating were also prepared, and the corresponding rate performance are presented in Figure S3 (Supporting Information). The rate capabilities of S-L and Mix electrode are significantly lower compared to the capacities of the S-Dry-L and Mix-Dry-Mix electrodes, not to mention when compared with the performance of L-Dry-S electrode. The reason for the electrochemical differences between the electrodes with and without drying process can be attributed to the interface between the two layers.[37] Take L-S model as an example, the first coating layer remains a sticky state when the second coating layer is applied, leading to a mixture of large and small particles at the boundary owing to gravity, which can be named as L-Mix-S. Compared to L-Dry-S, the tortuosity of L-S (L-Mix-S) model is higher, resulting in uneven electrochemical reaction kinetics and reduced rate performance.[38]

In order to meet the demands of industrialization, it is imperative for the electrode design to ensure uniform thickness across the coating area, thereby minimizing material wastage. Consequently, we have undertaken relevant research aimed at enhancing the utilization rate of double-layer architecture electrodes. Case I means the width of the second layer (S) is within the range of the first layer (L) (Figure 3e). We have selected three regions from the center to the edge for uniformity comparison, labeled as i, ii, and iii. Figure 3g demonstrates that the thicknesses of L-Dry-S electrodes gradually decrease from region i to region iii. Contrary to Case I, the width of the second coating layer is outside the range of the first layer in Case II (Figure 3f). As performed in Figure 3h, from region i to region iii, the electrode thicknesses are not much different, presenting a uniform electrode thickness distribution.

2.4. Porosity Investigation on Double-Layer Architecture Electrode

Electrode calendaring is a crucial pre-processing step for thick electrode application, as it not only enhances the volumetric energy density of electrode materials but also mitigates the impact of electronic conductivity on the rate performance

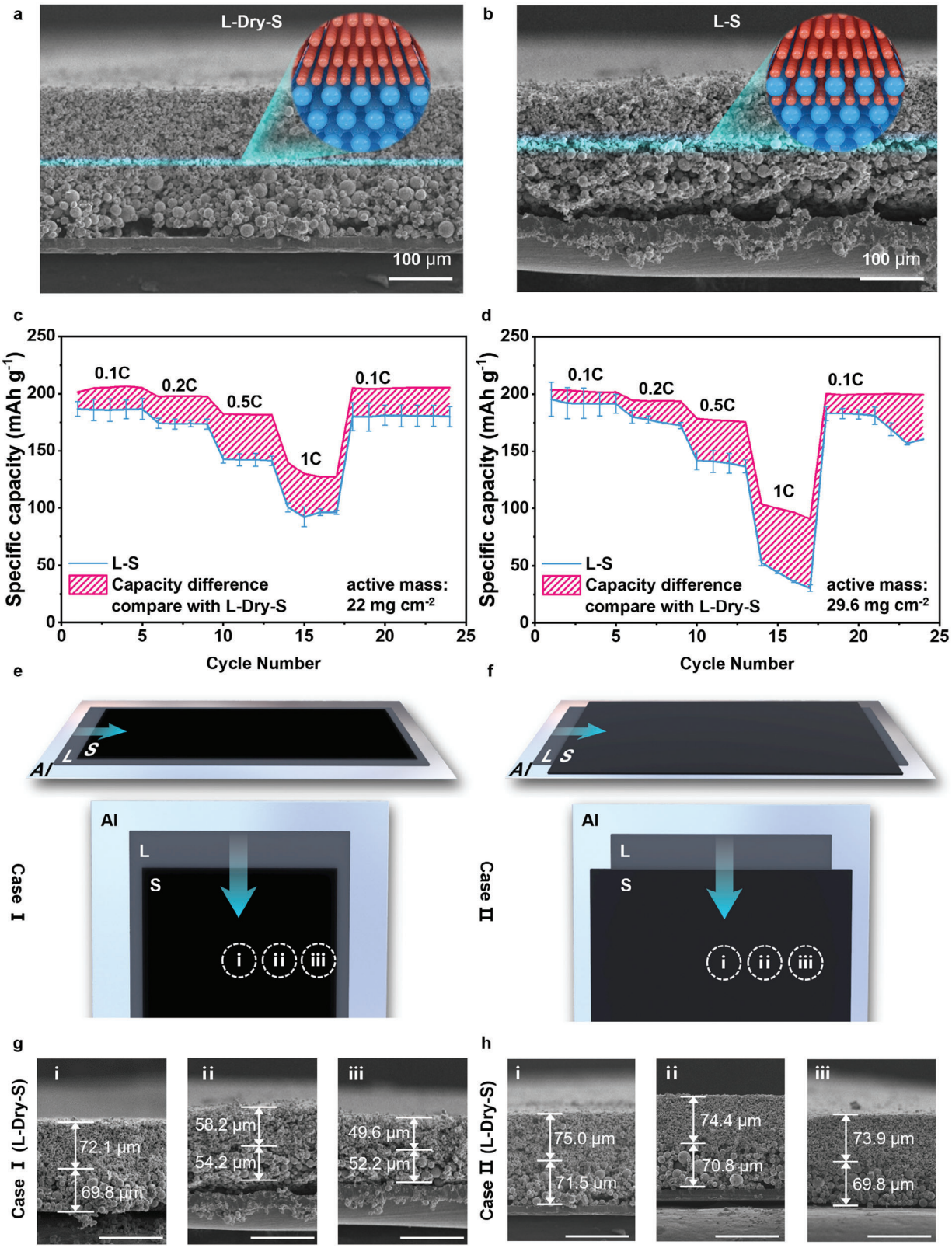

Figure 3. Investigation of manufacturing techniques for double-layer architecture electrodes. a,b) Cross-sectional images of the L-Dry-S electrode (a) and L-S electrode (b). The corresponding electrode loading is ≈29.6 mg cm^{-2}. c,d) Rate performance of S-L electrodes with different loadings, including 22 mg cm^{-2} (c) and 29.6 mg cm^{-2} (d). e,f) Schematic of the coating processes, including Case I (e) and Case II (f). g,h) Cross-sectional images of region i, ii, and iii in Case I (g) and Case II (h). The scale bar is 100 μm.

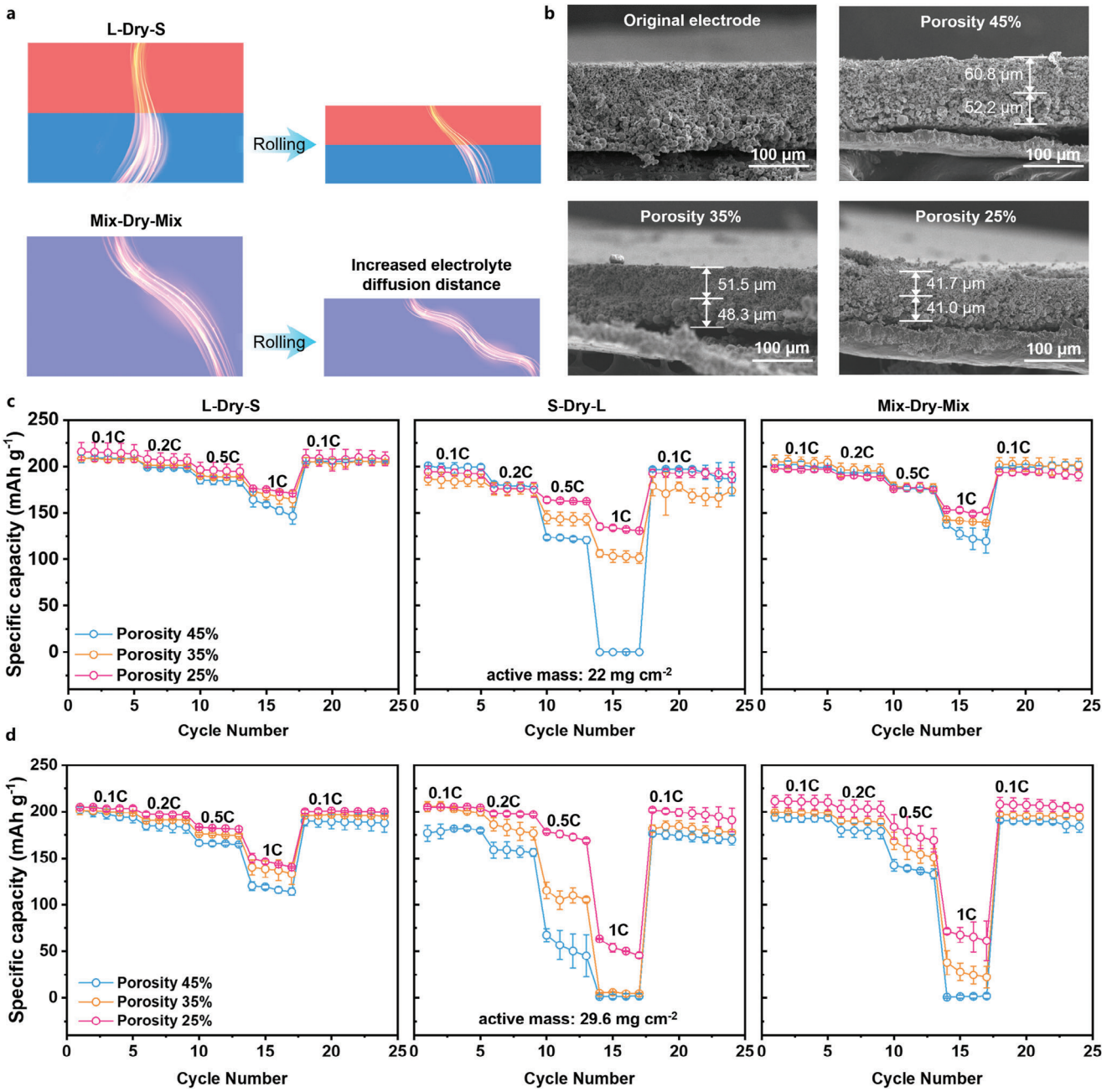

Figure 4. Double-layer architecture electrode porosity investigation. a) Schematic of the calendaring process, including traditional electrode and L-Dry-S electrode. b) Cross-sectional images of NMC83 with different porosities (45%, 35%, and 25%), the corresponding electrode structure is L-Dry-S. c,d) Rate performance of L-Dry-S, S-Dry-L, and Mix-Dry-Mix electrodes with loading of 22 mg cm^{-2} (c) and 29.6 mg cm^{-2} (d) at different porosities.

of high-loading electrodes by reducing the electronic transport distance.[39–42] Therefore, minimizing the unoccupied space within the electrode is desirable, however, excessive calendaring can impede lithium ion diffusion and compromise the electrode material's capacity. Hence, it is imperative to design an optimized electrode structure that ensures low porosity while achieving superior electrochemical performance (**Figure 4a**). As presented in Figure 4b, a calendar process was carried out on the prepared electrode. As to the L-Dry-S model, the electrode thickness changes from 141.5 to 82.7 μm, corresponding to the porosity variation from 55% to 25% (The calculation process of electrode thickness and porosity is referred to Table S1, Supporting Information).

Rate capabilities of the L-Dry-S, S-Dry-L, and Mix-Dry-Mix electrodes were performed under different porosities and loadings. In general, the rate performance of L-Dry-S electrode is significantly better than that of Mix-Dry-Mix and S-Dry-L (Figure 4c,d). Specifically, when the electrode loading is controlled at 22 mg cm^{-2} (Figure 4c), the specific discharge capacities of L-Dry-S, Mix-Dry-Mix, and S-Dry-L with 25% porosity at 1C are 176.10,

153.15, and 134.95 mAh g^{-1}, respectively. When the electrode loading increases to 29.6 mg cm^{-2}, the corresponding discharge capacities of the three electrodes present a decreasing trend, especially at high current densities. For instance, the discharge capacities of the three electrodes with 25% porosity at 1C are 150.05, 71.35, and 63.35 mAh g^{-1} (Figure 4d). At low porosity conditions, the high electrochemical performance of the L-Dry-S electrode can be attributed to the designed electrode structure. As depicted in Figure 4a, after undergoing a thorough calendaring process, the traditional electrode exhibits reduced porosity and increased void tortuosity, thereby impeding the diffusion rate of lithium ions within the electrode. Consequently, an increase in current results in a diminished discharge capacity. However, our designed electrode structure (L-Dry-S) features a double-layer void distribution. In the upper region with small particles, the calendaring process enhances lithium-ion transport paths, leading to concentration polarization that can be mitigated through adequate electrolyte supply. As the electrolyte continues to permeate downward, the large pores in the region of large particles facilitate the diffusion of lithium ions. This fast diffusion channel guarantees the rapid diffusion process of lithium ions within the thick electrode.

The electronic conductivity is also a crucial factor that influences the performance of electrode rate under high-loading conditions.[43] With nearly identical porosities (uncalendared, almost the same thickness), both the S-Dry-L electrode and Mix-Dry-Mix electrode exhibit zero discharge capacities at 1C (Figure 2g), but not in the L-Dry-S electrode. Moreover, after being calendared, the high loading S-Dry-L and Mix-Dry-Mix electrodes still present 0 discharge capacity (Figure 4d), indicating that electronic conductivity does not limit capacity release.[35]

2.5. The Optimum Thickness Ratio of the Double-Layer Architecture Electrode

To fully exploit the potential of the double-layer architecture electrode, we also investigated the impact of different layer thickness ratios on the electrochemical performance. To ensure a consistent electrode load, we adjusted the thickness of both the upper and lower layers of the L-Dry-S electrode. As depicted in **Figure 5a–c**, the thickness of the L layer gradually increases until most of the electrode is taken up by the large particles, and the corresponding thickness ratios between the L and S layers can be approximated as 3:7, 5:5, and 7:3. The rate capability was evaluated for the three different structures, and it was observed that the L-Dry-S electrode with a ratio of 7:3 exhibited superior performance, particularly at 1C (134.95 mAh g^{-1}) (Figure 5d). In parallel, the feasibility of the double-layer electrode structure (L:S = 1:1) relative to the conventional single electrode structure (L:S = 0:1) was verified under long cycling in full-cell configuration, as illustrated in Figure 5h,i. There was no significant disparity in specific capacity between L:S = 1:1 and L:S = 0:1 at a charge/discharge rate of 0.1C; however, this discrepancy arises at 0.5C. At higher current densities, a notable distinction exists in the specific capacity between the two electrodes (Figure 5h). Moreover, Figure 5i presents the typical charge/discharge curves of graphite||NCM83 full cells during 200 cycles at 0.5C between 2.7 and 4.3 V. In the case of L:S = 0:1, the polarization of the electrochemical reactions gradually aggravates with the increase of cycling number, as indicated by the gradual ascent/ descent of charge/discharge voltage platforms.[31,32] However, the prepared double-layer electrode structure L:S = 1:1 effectively suppresses the polarization aggravation of the cells since there are only slight changes in the voltage platforms with the increase of cycling number. This can be attributed to the uneven tortuosity resulting from the small particle size of L:S = 0:1, which impedes electrolyte penetration and hampers sufficient diffusion of lithium ions within the electrode structure, consequently leading to decreased capacity. Conversely, our electrode design with an L:S ratio of 1:1 demonstrates commendable cycling stability owing to its smooth electrolyte recharge pathway, which facilitates the rapid diffusion of lithium ions even under high current density conditions.

To further validate the experimental findings, multi-physics simulations were carried out on different L/S ratios, including 3:7, 4:6, 5:5, 6:4, and 7:3 (Figure 5e). The electrolyte density, electrolyte viscosity, and electrode loading were set as 1.2 g cm^{-3}, 3.1 cp,[44–47] and 30 mg cm^{-2}, respectively. The simulation results are demonstrated in Figure 5f. The top boundary of the region is set as a velocity inlet where only the electrolyte is injected as a fluid and the fluid velocity is 10^{-4} m s^{-1}, and the bottom boundary of the region is set as the outlet (Video S3–S7, Supporting Information). The values of 1% VOF were collected for comparison. With the increase of L layer (large particle) thickness, there is a gradual decrease in the value of 1% VOF, reaching its minimum when the ratio of L to S is 7:3. The results demonstrate that an increase in the proportion of large particle size and a decrease in the proportion of small particle size are conducive to the rapid wetting of electrolyte and the diffusion of lithium ions. This leads to a significant improvement in the multiplicative performance and cycling performance. However, an excess of large particle size will result in a reduction in the volumetric energy density of the single cell. Consequently, the investigation of the optimal thickness ratio is of great utility in identifying a suitable L/S ratio that meets the consumer's demand for high energy density while maintaining excellent rate performance and cycling performance.

These findings provide two suggestions: 1) In the industrial preparation process of high-loading electrodes, it is necessary to incorporate a mixture of large and small particles to improve the volume energy density. Under such conditions, separate coatings of large and small particles along with implementation of the L-Dry-S model can greatly enhance the rate capability. 2) Under the premise that the volume energy density is not affected, minimizing the S-layer thickness in the L-Dry-S model improves electrode rate performance.

2.6. Concentration Polarization Minimization Mechanism

Before the large-scale application of thick electrodes, the rate performance must be enhanced at first. Only by clarifying the underlying causes of the poor kinetics performance for the thick electrodes, can there be a theoretical basis to increase the rate capability. When there is a current flowing through the electrodes, it will be polarized due to different types of resistances, causing the decrease of capacity. Three of these resistances are important: ohmic resistance caused by solid-phase electron transport,

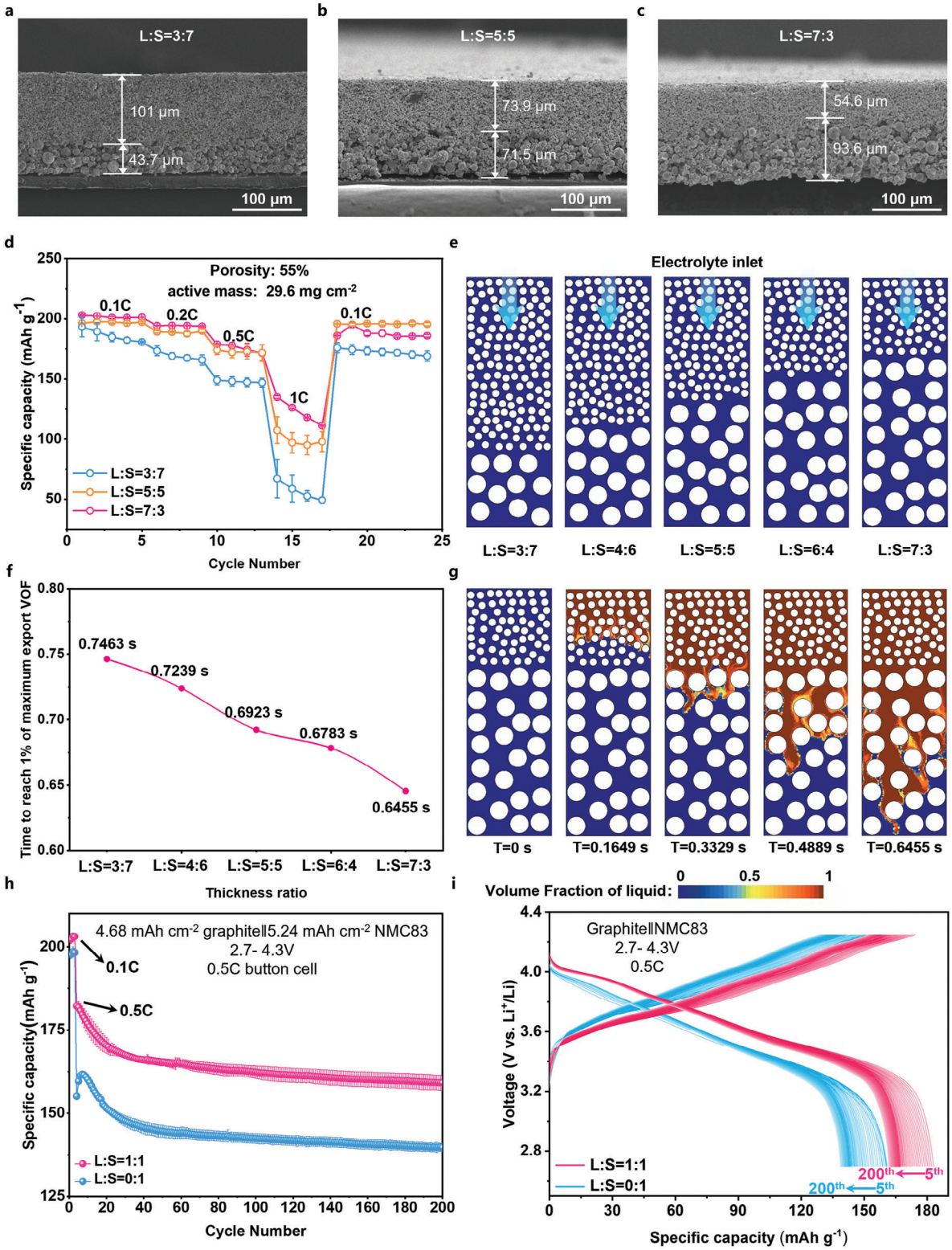

Figure 5. Optimal thickness ratio screening. a–c) Cross-sectional images of the L-Dry-S electrodes with different L/S thickness ratios, including 3:7 (a), 5:5 (b), and 7:3 (c). The corresponding electrode loading is ≈29.6 mg cm^{-2}. d) Rate performance of NMC83 electrodes (L-Dry-S) with different L/S thickness ratios. e) Simulation model of L-Dry-S electrodes with different L/S thickness ratios. f) Time to reach 1% of maximum export VOF of the five kinds of L-Dry-S electrodes with different L/S thickness ratios. g) Electrolyte infiltration processes in the L-Dry-S electrode with the L/S thickness ratios of 7:3. h) Cycling performance of NMC 83 electrodes (L:S = 1:1 and L:S = 0:1) with loadings of 24.6 mg cm^{-2}. (1C = 210 mA g^{-1}). i) The typical charge/discharge curves of graphite||NCM811 full cells during the 200 cycles at 0.5C rate between 2.7–4.3 V with L:S = 1:1 and L:S = 0:1.

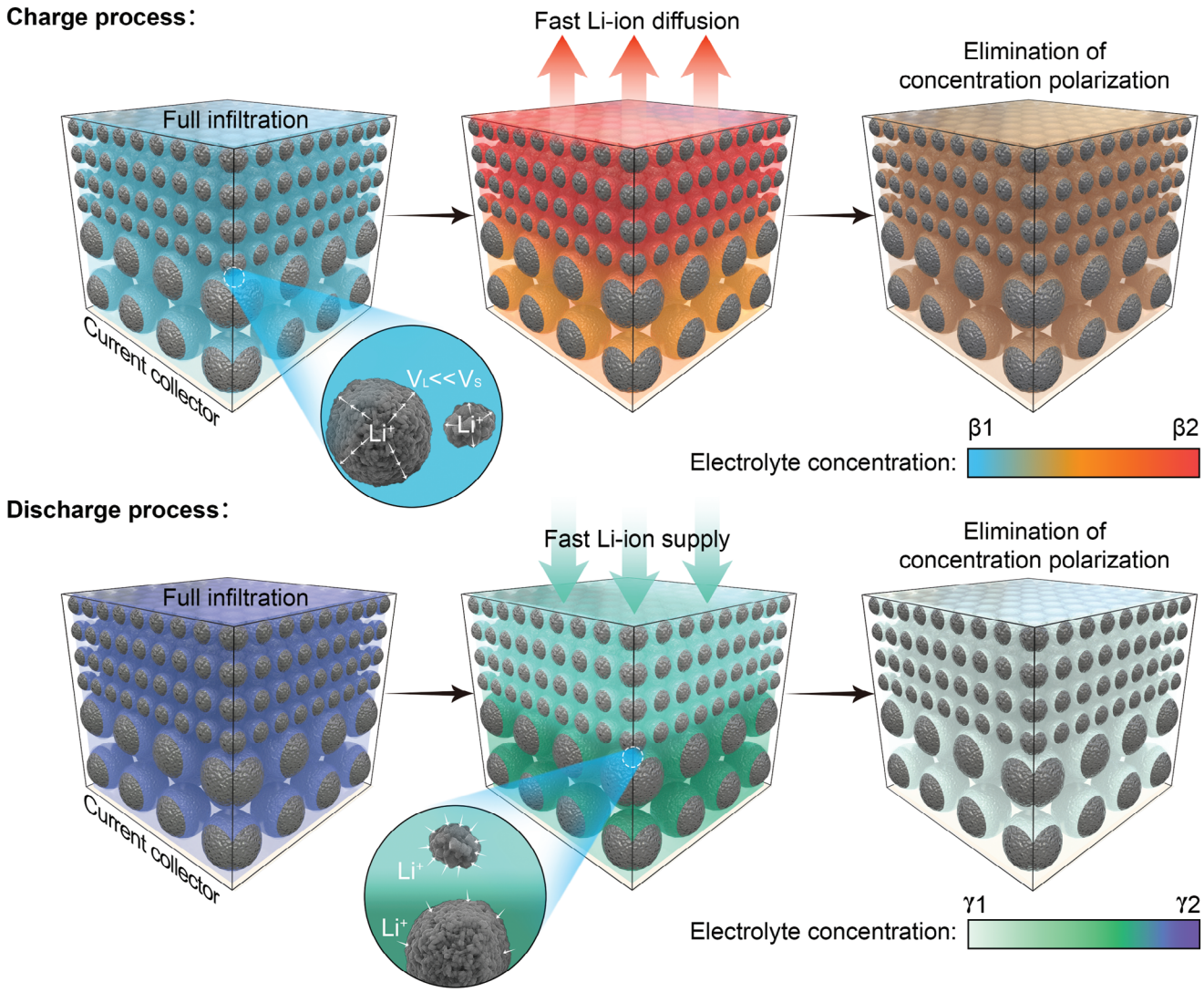

Figure 6. The mechanism of the mitigated concentration polarization of the L-Dry-S electrode.

liquid-phase ionic transport resistance, and charge transfer resistance at the interface between material and electrolyte. Compared with the electron transport and interfacial charge transfer,[48,49] liquid-phase ionic transport is slower, which is mainly considered as the rate-determining step for the sluggish electrochemical reaction kinetics of thick electrodes.

The essence of liquid-phase concentration polarization is that the Li^+ concentration will be in gradient distribution in the electrolyte in electrode pores when the current is applied, which becomes more pronounced at higher currentsor beyond a certain C-rate.[17,50,51] Taking the discharge process as an example, Li^+ concentration will decrease from the separator side of electrodes along the thickness direction. According to the Fick's law ($J = -D\frac{\partial C}{\partial n}$), there exists an ionic limited diffusion distance (n).[13] The concentration polarization increases appreciably with electrode thickness owing to limited diffusion distance (n) can't meet the actual internal diffusion distance of the electrode.[23,34,52,53] In this study, the electrode structure was optimized to address the issue of concentration polarization within the thick electrode, including L-Dry-S, S-Dry-L, and Mix-Dry-Mix, and the L-Dry-S electrode structure exhibits excellent ability in alleviating the concentration polarization.

As illustrated in **Figure 6**, the electrolyte concentration within the L-Dry-S electrode was uniformly distributed during the electrochemical processes. In the charge process, owing to the disparate diffusion speeds of lithium ions (V_L<<V_S), the lithium ions within the small particle diffuse rapidly into the electrolyte at the commencement of charging, whereas the lithium ions within the large particle diffuse at a relatively slow rate. Therefore, the L-Dry-S electrode structure forms a concentration gradient with a high concentration of lithium ions in the electrolyte near the small particle and a low concentration of lithium ions in the electrolyte near the large particle. Fortunately, the small particle is in full contact with the electrolyte, due to Fick's law the high concentration of lithium ions is able to diffuse into the electrolyte rapidly, and the concentration polarization is eliminated during the charging process. During the discharge process, the lithium ions start to intercalate into the cathode material, and since the

small particle can intake more lithium ions at the same time than large particles, the L-Dry-S electrode structure forms a concentration gradient of low lithium ion concentration near the small particle and high lithium ion concentration near the large particle at the beginning of the discharge. However, the small particle can receive a continuous supply of electrolyte, and the low lithium ion concentration is replenished, which in turn mitigates the concentration polarization. On the other hand, neither S-Dry-L (Figure S6, Supporting Information) nor Mix-Dry-Mix (Figure S7, Supporting Information) can alleviate the concentration polarization phenomenon well in the charging and discharging processes. Therefore, the well balance of electrolyte diffusion channel and lithium ion reaction speeds can effectively minimize the electrode concentration polarizion for high power batteries.

3. Conclusion

In summary, we have developed a double-layer architecture electrode featuring a fast electrolyte diffusion channel, which effectively addresses the polarization issue of the commercial high-loading electrode. With the L-Dry-S electrode structure, the corresponding high-loading electrode demonstrates 73.3% (150.0 mAh g^{-1}) capacity retention at 1C compared to the 0.1C capacity with 25% electrode porosity, superior than that of the traditional Mix electrode. Furthermore, we have also discussed the principles behind double-layer architecture electrode design, including coating protocol, porosity adjustment, and thickness optimization for different layers. In addition, it should be noted that the design of minimized cathode Li-ion concentration polarization can also be applied to other battery materials such as $LiFePO_4$, silicon, and graphite. This study is expected to have practical implications in the field of industry, aiming to alleviate consumer concerns regarding battery charging durations.

4. Experimental Section

Characterization: The morphologies of NMC83 and the cross-section images of NMC83 electrode were investigated by scanning electron microscopy (SEM, HITACHI) at voltage of 10 kV. The diffusion rates of electrolytes in different electrodes were captured by the distribution of P element by EDS mapping (HITACHI). The corresponding voltage and take off angles are 15 kV and 35.0°. Measuring electrolyte wettability and Li^+ diffusion coefficient by electrochemical impedance spectroscopy. EIS was performed using a CHI660. Spectra were recorded at a frequency range of 1 MHz–0.1 Hz, with a quiet time of 2 s and an amplitude of 5 mV.

Cell Preparation: The active material NMC83 ($LiNi_{0.83}Mn_{0.12}Co_{0.05}O_2$) was blended with acetylene carbon black (Shenzhen Kejing Star Technology Company) and polyvinylidene difluoride (PVDF, Shenzhen KeJing Star Technology Company) with a weight ratio of 96:2:2 in N-methyl pyrrolidone (NMP, Macklin) solution and stirred in a Thinky machine to prepare electrode slurry. The slurry was then coated onto an Al foil using a coating machine. After drying overnight in a vacuum at 80 °C, the electrodes were punched into 0.785 cm^2 disks. Here, the electrode thicknesses were controlled at 22 and 29.6 mg cm^{-2}, respectively. The porosities of the original electrodes without calendaring were between 55% and 60%, which was labeled as 55%. Thick electrodes with different porosities (25%, 35%, and 45%) were prepared by calendaring the electrodes to the corresponding thickness. Porosity was calculated by [1-(0.96*m/ρ_{active} + 0.02*m/ρ_c + 0.02*m/ρ_{pvdf})/SH] (m is the total mass coating on current collector; ρ_{active}, ρ_c, and ρ_{pvdf} are the densities of active material, conductive carbon and PVDF; S is the area of the electrode; H is the thickness of the electrode materials on the current collector.) 1 M $LiPF_6$ in ethyl carbonate (EC) and methyl carbonate (EMC) (3:7 by weight) with 2% VC as an additive was used as the electrolyte. $LiPF_6$, EC, and EMC were purchased from DoDoChem. The CR2032 coin half-cells were assembled with NMC83 electrode as cathodes, polypropylene (PP) as separator, and lithium foil (15.6 mm diameter, Cellithium Corporation) as an anode. The CR2032 coin full-cells were assembled with NMC83 electrode as cathodes, polypropylene (PP) as a separator, and Graphite as an anode. The electrolyte content was controlled at 70 µL. The moisture and oxygen contents were controlled lower than 1 ppm. The electrochemical performance of the coin cells was evaluated using Land tester. All the cells were tested between 2.7 and 4.3 V versus Li^+/Li at different current densities, and the 1C rate corresponds to 210 mA g^{-1}.

Double-Layer Architecture Electrode Fabrication: Here, two kinds of NMC83 particles were employed to fabricate double-layer architecture electrode, and the corresponding particle sizes are 4.5 and 11.3 µm, which were labeled as S and L, respectively. The double-layer architecture electrodes have two layers, with large particles on the bottom (L-S) or large particles on top (S-L). If there was a drying process (80 °C for 12 h) after the first layer coating, the corresponding electrodes are named as L-Dry-S or S-Dry-L. The traditional electrode was also prepared by coating a mixture of large and small particles for comparison. The electrodes with the mixture were labeled as Mix and Mix-Dry-Mix based on the inclusion of a drying process. Before assembled into the cells, all the prepared electrodes were dried at 110 °C in a vacuum oven for 12 h. For the coating details of L and S layers, take L-DRY-S as an example, the base of the first layer of L is aluminum foil, and the thickness ratio before and after drying can be used as an empirical formula to calculate the thickness of the first layer of this coating, while the base of the second layer of S is the L of the first layer. The first layer will absorb part of the NMP in the slurry, changing the rheology of the slurry, and then changing the thickness ratio of the second layer before and after drying. Therefore, the coating of L and S layers cannot be achieved by the same amount of slurry, but under the condition that the thickness of the first layer is determined, the coating thickness of the second layer is adjusted step by step, and the thickness ratio of L:S is finally maintained to be 1:1, which is verified by SEM electrode cross-section data. For L-S, the first layer of L is not dried after coating, causing compression and outward spreading due to gravity. This results in a reduction in the thickness of the first layer, leading to an increased paste thickness prior to its application. Additionally, during the coating of the second layer, there is an occurrence of particle mixing between small and large particles under gravity's influence. Consequently, adjustments are required for the corresponding thickness of the second layer slurry. For details, please refer to Table S2 (Supporting Information).

Volume of Fluid (VOF) Method: The VOF model was a widely utilized method in two-phase computational fluid dynamics (CFD) simulations, known for its simplicity and suitability in simulating flows of multiple immiscible fluids on numerical grids capable of resolving the interface between the phases. It is suitable for solving problems involving immiscible fluid mixtures, free surfaces, and phase contact time. In such cases, there is no need for extra modeling of interphase interaction, and the model assumption that all phases share velocity, pressure, and temperature fields becomes a discretization error. The mass, momentum, and energy equations can be expressed as follows:

$$\frac{\partial}{\partial t}(\rho) + \nabla \cdot (\rho \vec{u}) = 0 \tag{1}$$

$$\frac{\partial}{\partial t}(\rho \vec{u}) + \nabla \cdot (\rho \vec{u}\vec{u}) = -\nabla p + \nabla \cdot \left[\mu \left(\nabla \vec{u} + \nabla \vec{u}^T\right)\right] + \rho \vec{g} + \vec{F}_s \tag{2}$$

where $\vec{u}$, p, ρ, μ, and $\vec{g}$ are the fluid velocity, pressure, fluid density, fluid viscosity, and gravitational acceleration, respectively.

The VOF multiphase model implementation in Simcenter STAR-CCM+ assumes that the mesh resolution is sufficient to resolve the position and the shape of the interface between the phases. The distribution of phases and the position of the interface are described by the fields of phase volume fraction. The volume fraction of phase i is defined as:

$$\alpha_i = \frac{V_i}{V} \tag{3}$$

where V_i is the volume of phase i in the cell and V is the volume of the cell. The volume fractions of all phases in a cell must sum up to one:

$$\sum_{i=1}^{N} \alpha_i = 1 \quad (4)$$

where N is the total number of phases. Depending on the value of the volume fraction, the presence of different phases or fluids in a cell can be distinguished: 1) $\alpha_i = 0$ means the cell is completely void of phase i; 2) $\alpha_i = 1$ means the cell is completely filled with phase i; 3) $0 < \alpha_i < 1$ means values between the two limits indicating the presence of an interface between phases.

In this simulation, first order discretization scheme and pressure-velocity coupling model were used. 2D simulations were used to ease the numerical difficulty. The height of the region in the simulation was 146 µm and the width was 50 µm. First order implicit scheme was applied for transient formulation and the time interval was set as 1×10^{-4} s for $t < 0.1$ s and 2×10^{-4} s for $t > 0.1$ s. The boundary and initial condition were set as follows: the top boundary of the region was set as a velocity inlet where only the electrolyte was injected as a fluid and the fluid velocity is 10^{-4} m s^{-1}; the bottom boundary of the region is set as outlet; and the left and right boundaries of the region are set as symmetric plane.

To assess the model's sensitivity, two sets of meshes were employed, and a comparison between them was conducted. As illustrated in Figure S5 (Supporting Information), the coarse mesh successfully captures fluid motion but exhibits a more ambiguous boundary. In contrast, the finer mesh provides a much clearer boundary. Consequently, a finer mesh was selected for this study. The base size of the coarse mesh was set at 1×10^{-5} m, while the base size of the fine mesh is 1×10^{-6} m. Additionally, to enhance accuracy, three boundary layers with a combined thickness of 1×10^{-7} m were introduced in the vicinity of the particle surface.

Supporting Information

Supporting Information is available from the Wiley Online Library or from the author.

Acknowledgements

The authors are grateful to the financial support of National Natural Science Foundation (NNSF) of China (Nos. 52202269, 52002248, U23B2069), Project of Department of Education of Guangdong Province (No. 2022ZDZX3018), Basic and Applied Basic Research Foundation of Guangdong Province (No. 2021B1515130002), Guangdong Key Laboratory of Design and calculation of New Energy Materials (No. 2017B030301013), Shenzhen Key Laboratory of New Energy Resources Genome Preparation and Testing (No. ZDSYS201707281026184), Shenzhen Science and Technology program (No. 20220810155330003, NO. KJZD20230923115005009), Shenzhen Basic Research Project (No. JCYJ20190808163005631), and Xiangjiang Lab (22XJ01007) for providing financial support for this work. The authors are grateful to the Instrumental Analysis Center of Shenzhen University (Xili Campus) for providing the facilities for the material analyses.

Conflict of Interest

The authors declare no conflict of interest.

Author Contributions

W.C. and K.W. contributed equally to this work. J.H. and Q.Z. performed conceptualization, W.C., J.C., H.W., L.L., H.L., X.R., X.O.B.X. performed methodology, K.W.and Y.L. performed formal analysis, J.H., Q.Z., and J.L. did supervision, J.H. and Q.Z. acquired funding, J.H. and W.C. wrote the original draft, B.X., F.P. and, J.H. wrote- review and perform editing.

Data Availability Statement

The data that support the findings of this study are available from the corresponding author upon reasonable request.

Keywords

concentration polarization, electrode structure design, electrolyte diffusion channel, high-power lithium batteries

Received: June 23, 2024
Revised: August 12, 2024
Published online: September 5, 2024

[1] M. Zhang, M. Chouchane, S. A. Shojaee, B. Winiarski, Z. Liu, L. Li, R. Pelapur, A. Shodiev, W. Yao, J.-M. Doux, S. Wang, Y. Li, C. Liu, H. Lemmens, A. A. Franco, Y. S. Meng, *Joule* **2023**, *7*, 201.
[2] Y. Kuang, C. Chen, D. Kirsch, L. Hu, *Adv. Energy Mater.* **2019**, *9*, 1901457.
[3] J. Liu, Z. Bao, Y. Cui, E. J. Dufek, J. Goodenough, P. G. Khalifah, Q. Li, B. Y. Liaw, P. Liu, A. Manthiram, Y. S. Meng, V. R. Subramanian, M. F. Toney, V. V. Viswanathan, M. S. Whittingham, J. Xiao, W. Xu, J. Yang, X. Q. Yang, J. G. Zhang, *Nat. Energy* **2019**, *4*, 180.
[4] H. Cui, Y. Song, D. Ren, L. Wang, X. He, *Joule* **2023**, *8*, 29.
[5] Q.-S. Liu, H.-W. An, X.-F. Wang, F.-P. Kong, Y.-C. Sun, Y.-X. Gong, S.-F. Lou, Y.-F. Shi, N. Sun, B. Deng, J. Wang, J.-J. Wang, *Natl. Sci. Rev.* **2023**, *10*, nwac272.
[6] M. Xu, B. Reichman, X. Wang, *Energy* **2019**, *186*, 115864.
[7] Y. Zhang, J. C. Kim, H. W. Song, S. Lee, *Nanoscale* **2023**, *15*, 4195.
[8] S. Lin, Y. Wang, Y. Chen, Z. Cai, J. Xiao, T. Muhmood, X. Hu, *Small* **2021**, *18*, 2104224.
[9] J. Wang, M.-m. Wang, N. Ren, J.-m. Dong, Y. Li, C.-h. Chen, *Energy. Storage. Mater.* **2021**, *39*, 287.
[10] B. Shi, Y. Shang, Y. Pei, S. Pei, L. Wang, D. Heider, Y. Zhao, C. Zheng, B. Yang, S. Yarlagadda, T. W. Chou, K. K. Fu, *Nano. Lett.* **2020**, *20*, 5504.
[11] X. Yang, K. Doyle-Davis, X. Gao, X. A. Sun, *eTransportation* **2022**, *11*, 100152.
[12] Y. D. Wu, N. N. He, G. J. Liang, C. F. Zhang, C. H. Liang, D. Ho, M. Z. Wu, H. B. Hu, *Adv. Funct. Mater.* **2024**, *34*, 2301734.
[13] Y. Guo, X. Li, H. Guo, Q. Qin, Z. Wang, J. Wang, G. Yan, *Energy. Storage. Mater.* **2022**, *51*, 476.
[14] R. He, G. Tian, S. Li, Z. Han, W. Zhong, S. Cheng, J. Xie, *Nano. Lett.* **2022**, *22*, 2429.
[15] J. Wu, Z. Ju, X. Zhang, X. Xu, K. J. Takeuchi, A. C. Marschilok, E. S. Takeuchi, G. Yu, *ACS Nano* **2022**, *16*, 4805.
[16] J. Wu, Z. Ju, X. Zhang, A. C. Marschilok, K. J. Takeuchi, H. Wang, E. S. Takeuchi, G. Yu, *Adv. Mater.* **2022**, *34*, 2202780.
[17] Z. Ju, Y. Zhu, X. Zhang, D. M. Lutz, Z. Fang, K. J. Takeuchi, E. S. Takeuchi, A. C. Marschilok, G. Yu, *Chem. Mater.* **2020**, *32*, 1684.
[18] X. Zhang, Z. Hui, S. King, L. Wang, Z. Ju, J. Wu, K. J. Takeuchi, A. C. Marschilok, A. C. West, E. S. Takeuchi, G. Yu, *Nano. Lett.* **2021**, *21*, 5896.
[19] Y. Zhu, Z. Y. Ju, X. Zhang, D. M. Lutz, L. M. Housel, Y. G. Zhou, K. J. Takeuchi, E. S. Takeuchi, A. C. Marschilok, G. H. Yu, *Adv. Mater.* **2020**, *32*, 2070074.
[20] J. Wu, Z. Ju, X. Zhang, C. Quilty, K. J. Takeuchi, D. C. Bock, A. C. Marschilok, E. S. Takeuchi, G. Yu, *ACS Nano* **2021**, *15*, 19109.
[21] X. Li, Y. Zhang, S. Wang, Y. Liu, Y. Ding, G. He, N. Zhang, G. Yu, *Nano. Lett.* **2019**, *20*, 701.

[22] A. Shodiev, M. Chouchane, M. Gaberscek, O. Arcelus, J. Xu, H. Oularbi, J. Yu, J. Li, M. Morcrette, A. A. Franco, *Energy. Storage. Mater.* **2022**, *47*, 462.
[23] Y. Liu, Y. Zhu, Y. Cui, *Nat. Energy* **2019**, *4*, 540.
[24] J. Yang, Y. Li, A. Mijailovic, G. Wang, J. Xiong, K. Mathew, W. Lu, B. W. Sheldon, Q. Wu, *J. Mater. Chem. A* **2022**, *10*, 12114.
[25] X. Zhang, Z. Hui, S. T. King, J. Wu, Z. Ju, K. J. Takeuchi, A. C. Marschilok, A. C. West, E. S. Takeuchi, L. Wang, G. Yu, *Nano. Lett.* **2022**, *22*, 2521.
[26] Y.-K. Sun, H.-B. Kang, S.-T. Myung, J. Prakash, *J. Electrochem. Soc.* **2010**, *157*, A1335.
[27] S. N. Lauro, J. N. Burrow, C. B. Mullins, *eScience* **2023**, *3*, 100152.
[28] M. Wood, J. Li, Z. Du, C. Daniel, A. R. Dunlop, B. J. Polzin, A. N. Jansen, G. K. Krumdick, D. L. Wood, *J. Power. Sources.* **2021**, *515*, 230429.
[29] L. L. Lu, Y. Y. Lu, Z. X. Zhu, J. X. Shao, H. B. Yao, S. G. Wang, T. W. Zhang, Y. Ni, X. X. Wang, S. H. Yu, *Sci. Adv.* **2022**, *8*, eabm6624.
[30] F. J. Günter, J. B. Habedank, D. Schreiner, T. Neuwirth, R. Gilles, G. Reinhart, *J. Electrochem. Soc.* **2018**, *165*, A3249.
[31] Y. Li, Q. Qu, L. Lv, J. Shao, H. Zheng, *Adv. Funct. Mater.* **2024**, *34*, 2314100.
[32] R. Zhang, C. Wang, P. Zou, R. Lin, L. Ma, L. Yin, T. Li, W. Xu, H. Jia, Q. Li, S. Sainio, K. Kisslinger, S. E. Trask, S. N. Ehrlich, Y. Yang, A. M. Kiss, M. Ge, B. J. Polzin, S. J. Lee, W. Xu, Y. Ren, H. L. Xin, *Nature* **2022**, *610*, 67.
[33] W. Huang, L. Yang, Z. Chen, T. Liu, G. Ren, P. Shan, B. W. Zhang, S. Chen, S. Li, J. Li, C. Lin, W. Zhao, J. Qiu, J. Fang, M. Zhang, C. Dong, F. Li, Y. Yang, C. J. Sun, Y. Ren, Q. Huang, G. Hou, S. X. Dou, J. Lu, K. Amine, F. Pan, *Adv. Mater.* **2022**, *34*, 2202745.
[34] J. Hu, Y. Jiang, S. Cui, Y. Duan, T. Liu, H. Guo, L. Lin, Y. Lin, J. Zheng, K. Amine, F. Pan, *Adv. Energy. Mater.* **2016**, *6*, 1600856.
[35] J. Hu, B. Wu, X. Cao, Y. Bi, S. Chae, C. Niu, B. Xiao, J. Tao, J. Zhang, J. Xiao, *J. Power. Sources.* **2020**, *454*, 227966.
[36] X. Gao, L. Wang, J. Guo, S. Li, H. Zhang, L. Chen, Y. Zhang, Y. Lai, Z. Zhang, *Adv. Funct. Mater.* **2024**, 2407692, https://doi.org/10.1002/adfm.202407692.
[37] C. Cheng, R. Drummond, S. R. Duncan, P. S. Grant, *J. Power. Sources.* **2019**, *413*, 59.
[38] S.-H. Park, P. J. King, R. Tian, C. S. Boland, J. Coelho, C. Zhang, P. McBean, N. McEvoy, M. P. Kremer, D. Daly, J. N. Coleman, V. Nicolosi, *Nat. Energy.* **2019**, *4*, 560.
[39] D. Schreiner, J. Lindenblatt, R. Daub, G. Reinhart, *Energy. Technol.* **2023**, *11*, 2200442.
[40] X. Lu, S. R. Daemi, A. Bertei, M. D. R. Kok, K. B. O'Regan, L. Rasha, J. Park, G. Hinds, E. Kendrick, D. J. L. Brett, P. R. Shearing, *Joule* **2020**, *4*, 2746.
[41] M. Abdollahifar, H. Cavers, S. Scheffler, A. Diener, M. Lippke, A. Kwade, *Adv. Energy. Mater.* **2023**, *13*, 2300973.
[42] R. Sim, S. Lee, W. Li, A. Manthiram, *ACS Appl. Mater. Interfaces.* **2021**, *13*, 42898.
[43] S. Xu, X. Tan, W. Ding, W. Ren, Q. Zhao, W. Huang, J. Liu, R. Qi, Y. Zhang, J. Yang, C. Zuo, H. Ji, H. Ren, B. Cao, H. Xue, Z. Gao, H. Yi, W. Zhao, Y. Xiao, Q. Zhao, M. Zhang, F. Pan, *Angew. Chem., Int. Ed.* **2023**, *62*, 202218595.
[44] E. R. Logan, E. M. Tonita, K. L. Gering, L. Ma, M. K. G. Bauer, J. Li, L. Y. Beaulieu, J. R. Dahn, *J. Electrochem. Soc.* **2018**, *165*, A705.
[45] Y. Zhang, Y. Katayama, R. Tatara, L. Giordano, Y. Yu, D. Fraggedakis, J. G. Sun, F. Maglia, R. Jung, M. Z. Bazant, Y. Shao-Horn, *Energy. Environ. Sci.* **2020**, *13*, 183.
[46] H. Jia, Y. Xu, S. D. Burton, P. Gao, X. Zhang, B. E. Matthews, M. H. Engelhard, L. Zhong, M. E. Bowden, B. Xiao, K. S. Han, C. Wang, W. Xu, *ACS Appl. Mater. Interfaces.* **2020**, *12*, 54893.
[47] B. Koo, H. Lee, S. Hwang, J. Lee, Y.-K. Han, K. H. Ahn, C. Lee, H. Lee, *J. Phys. Chem. C* **2023**, *127*, 18271.
[48] P. Wang, G. Zhang, X.-Y. Wei, R. Liu, J.-J. Gu, F.-F. Cao, *J. Am. Chem. Soc.* **2021**, *143*, 3280.
[49] P. Wang, H. Ye, Y. X. Yin, H. Chen, Y. B. Bian, Z. R. Wang, F. F. Cao, Y. G. Guo, *Adv. Mater.* **2019**, *31*, 1805134.
[50] S. A. Krachkovskiy, J. D. Bazak, P. Werhun, B. J. Balcom, I. C. Halalay, G. R. Goward, *J. Am. Chem. Soc.* **2016**, *138*, 7992.
[51] M. Klett, M. Giesecke, A. Nyman, F. Hallberg, R. W. Lindström, G. Lindbergh, I. Furó, *J. Am. Chem. Soc.* **2012**, *134*, 14654.
[52] M. Doyle, T. F. Fuller, J. Newman, *Electrochim. Acta.* **1994**, *39*, 2073.
[53] K. G. Gallagher, S. E. Trask, C. Bauer, T. Woehrle, S. F. Lux, M. Tschech, P. Lamp, B. J. Polzin, S. Ha, B. Long, Q. Wu, W. Lu, D. W. Dees, A. N. Jansen, *J. Electrochem. Soc.* **2015**, *163*, A138.